Journal of Materials Chemistry B

RSC Publishing

PAPER

Chitosan–halloysite nanotubes nanocomposite scaffolds for tissue engineering†

Cite this: *J. Mater. Chem. B*, 2013, **1**, 2078

Mingxian Liu,[a] Chongchao Wu,[b] Yanpeng Jiao,[a] Sheng Xiong[b] and Changren Zhou*[a]

This work developed novel chitosan–halloysite nanotubes (HNTs) nanocomposite (NC) scaffolds by combining solution-mixing and freeze-drying techniques, and aimed to show the potential application of the scaffolds in tissue-engineering. The hydrogen bonding and electrostatic attraction between chitosan and HNTs were confirmed by spectroscopy and morphology analysis. The interfacial interactions resulted in a layer of chitosan absorbed on the surfaces of HNTs. The determination of mechanical and thermal properties demonstrated that the NC scaffolds exhibited significant enhancement in compressive strength, compressive modulus, and thermal stability compared with the pure chitosan scaffold. But the NC scaffolds showed reduced water uptake and increased density by the incorporation of HNTs. All the scaffolds exhibited a highly porous structure and HNTs had nearly no effect on the pore structure and porosity of the scaffolds. In order to assess cell attachment and viability on the materials, NIH3T3-E1 mouse fibroblasts were cultured on the materials. Results showed that chitosan–HNTs nanocomposites were cytocompatible even when the loading of HNTs was 80%. All these results suggested that chitosan–HNTs NC scaffolds exhibited great potential for applications in tissue engineering or as drug/gene carriers.

Received 21st January 2013
Accepted 11th February 2013

DOI: 10.1039/c3tb20084a

www.rsc.org/MaterialsB

1 Introduction

One of the most critical problems for tissue engineering is to establish a scaffold capable of supporting three-dimensional tissue formation.[1,2] To achieve this goal, scaffolds must meet some specific requirements.[3] A high porosity with adequate pore size is necessary to facilitate cell seeding and nutrients' diffusion. Biodegradability and the rate of degradation are also essential factors, since scaffolds should be absorbed by the surrounding tissues accompanied by new tissue formation. Furthermore, the scaffold should be mechanically strong for supporting the body, especially when the new bone tissue grows. The micro-structures of these scaffolds range from hydrogels,[4] open-pore structures,[2] to fibrous matrices[5] and numerous natural and synthetic scaffold materials have been developed. Among these materials, biopolymers such as collagen, chitosan, and hyaluronic acid have gained considerable attention due to their biocompatibility, biodegradability, environmental-friendliness, and convenient processability.[6]

Chitosan is a promising scaffold material for various applications in tissue engineering.[7–12] It is a linear polysaccharide composed of randomly distributed β-(1-4)-linked D-glucosamine (deacetylated unit) and *N*-acetyl-D-glucosamine (acetylated unit). Chitosan is produced commercially by deacetylation of chitin. An extensive network of intra- and inter-hydrogen bonds of chitosan enables it to adopt a highly ordered structure. So chitosan is normally insoluble in common solvents.[13] However, in diluted acidic (pH < 6) aqueous solutions, the free amino groups on the chitosan skeleton are protonated, which results in the dissolution of chitosan. In addition, the high charge density in diluted acidic aqueous solution allows chitosan to form complexes such as films, scaffolds, fibers, *etc.* by ion interactions. Attributed to their high biocompatibility, biodegradability, non-antigenicity and adsorption properties, chitosan-based scaffolds are suitable for tissue engineering and drug delivery systems.[14] Chitosan and its complexes are easily fabricated into porous three-dimensional (3D) scaffolds by the techniques of electro-spinning or freeze-drying. The freeze-drying technology is one of the most common methods for preparing chitosan 3D scaffolds, which proceeds by first dissolving the chitosan in acetic acid medium and then lyophilization. More importantly, the properties of the scaffold, such as micro-structure, crystallinity, and mechanical strength, can be modulated by changing the freeze-drying conditions. However, the disadvantages of a pure chitosan scaffold are mechanical weakness and insufficient biological response, which limit their practical application in tissue engineering.

To achieve the goal of enhancing both the biological response and the mechanical properties, elaboration of

[a]*Department of Materials Science and Engineering, Jinan University, Guangzhou 510632, China. E-mail: tcrz9@jnu.edu.cn; Fax: +86(20)-85223271*

[b]*Biomedical R&D Center, Guangdong Provincial Key Laboratory of Bioengineering Medicine, National Engineering Research Center of Genetic Medicine, Jinan University, Guangzhou 510632, China*

† Electronic supplementary information (ESI) available. See DOI: 10.1039/c3tb20084a

nanocomposite (NC) scaffolds by combining biodegradable polymers with bioactive nanoparticles is one of the most promising solutions.[15] Owing to the strong interfacial interactions in these systems and the high strength of nanoreinforcement itself, chitosan nanocomposites show a wide range of tailored mechanical and biological properties. For example, nano-hydroxyapatite (HA) was combined with chitosan for forming organic–inorganic hybrid scaffolds by the lyophilization method.[8,12,16] The resulting NC scaffolds show highly porous structures and significantly superior physico-chemical, mechanical and biological properties compared to pure chitosan. Conducting carbon nanotube (CNTs)–chitosan 3D NC scaffolds with enhanced mechanical properties were also successfully prepared.[9] Bioactive glass ceramic nanoparticles,[17] nano TiO_2,[10] and graphene oxide (GO)[18] *etc.* were also used as nanoreinforcements for chitosan scaffolds. However, the used nanoparticles are either difficult to synthesize or complicate matters as they need to pre-treated before use, which limits their practical applications in tissue engineering. Exploring naturally available, cheap, high strength, and biocompatible nanoparticles for preparing chitosan NC scaffolds is often highlighted.

The environmental friendliness and biocompatible nature make halloysite nanotubes (HNTs) an important nanomaterial for developing new organic–inorganic nanocomposites. HNTs, with a chemical formula of $Al_2Si_2O_5(OH)_4 \cdot nH_2O$, is a dioctahedral 1 : 1 clay mineral that occurs widely in soils of wet tropical and subtropical regions and weathered rocks, being formed by weathering of many types of igneous and non-igneous rocks.[19] HNTs have a dominantly hollow tubular structure in the nanoscale with an aspect ratio of *ca.* 20. The length of HNTs is in the range of 0.2–1.5 μm, while the inner diameter and the outer diameter of tubes are in the ranges of 10–30 nm and 40–70 nm, respectively. The tubes have aluminum innermost and silicate outermost surfaces, which are positively and negatively charged, respectively. Due to the hydrophilicity of HNTs and the small dimensions, raw HNTs can be readily dispersed in water easily by mechanical stirring or ultrasonic treatment. Therefore, if one mixes HNTs with chitosan in dilute acidic solution, a chitosan–HNTs complex may be formed *via* electrostatic attractions. Also, the Al–O–H and silanols on the surfaces of HNTs can form hydrogen bonds with the amino-group and hydroxyl groups of chitosan. So, it is expected that chitosan has good interfacial compatibility with HNTs and HNTs can be easily dispersed in chitosan. However, little work has been done on the development of chitosan–HNTs nanocomposites.[20–22]

In the present work, we describe the first study of the structure–processing–property relationship in chitosan–HNTs NC scaffolds for tissue engineering application. Chitosan was mixed with HNTs in acidic aqueous solution to form a homogenous organic–inorganic hybrid, which was subsequently freeze-dried into a porous 3D scaffold. The resulting chitosan–HNTs NC scaffolds were characterized by Fourier transform infra-red spectroscopy, atomic force microscopy, scanning electron microscopy (SEM) and X-ray diffraction analysis. Additionally, the mechanical and thermal properties of chitosan–HNTs NC scaffolds were assessed by compression tests and thermogravimetry, respectively. The water adsorption, density and porosity of the chitosan–HNTs NC scaffolds were also determined. The intrinsic cytotoxicity of the chitosan and chitosan–HNTs nanocomposites was investigated by carrying out a cellular viability assay (MTT test) and fluorescence microscopy using mouse fibroblastic-like cells. The results suggest that incorporation of HNTs into chitosan can form a uniform 3D porous scaffold with enhanced physico-chemical, mechanical, thermal and biological properties for utilization in tissue engineering and drug/gene release applications.

2 Experimental

2.1 Raw materials

Chitosan was supplied by Jinan Haidebei Marine Bioengineering Co. Ltd. (China). Its deacetylation and viscosity-average molecular weight are 95% and 600 000 g mol^{-1}, respectively. HNTs were mined from Hunan province, China. The elemental composition of HNTs by X-ray fluorescence (XRF) was determined as follows (wt%): SiO_2, 54.29; Al_2O_3, 44.51; Fe_2O_3, 0.63; TiO_2, 0.006. Before use, HNTs were purified according to ref. 23. The Brunauer–Emmett–Teller (BET) surface area of the used HNTs was 50.4 m^2 g^{-1}. All other chemicals used in this paper were of analytical grade. Ultrapure water from Milli-Q water system was used to prepare the aqueous solutions.

2.2 Preparation of the chitosan–HNTs NC scaffold

The chitosan and chitosan–HNTs NC scaffolds were prepared by solution mixing and subsequent freeze-drying method. The typical procedure for preparing the NC scaffolds was as described below. 2 g chitosan was dissolved in 100 mL of 2 wt% acetic acid solution with mechanical stirring. Then the calculated amount of HNTs powder was added to the chitosan solution. The solution mixture was continuously stirred overnight and then treated by ultrasound for 1 hour at ambient temperature in order to obtain a good dispersion of HNTs. Then the solution was poured into a cylindrical plastic mould with 10 mm diameter and 10 mm height. Subsequently, it was frozen into ice at −20 °C overnight in a freezer and then lyophilized at −80 °C using a Christ freeze dryer ALPHA 2-4 LSC plus. For comparison, pure chitosan scaffolds were also prepared in the same way but without the addition of HNTs. The height and diameter of the obtained scaffold were both measured as ~10 mm. The sample codes of the NC scaffolds (CS2N1, CS1N1, CS1N2, CS1N4) represent the weight ratio of chitosan (CS) and HNTs (N). For example, CS1N2 represents that the weight ratio of chitosan and HNTs was 1 : 2 in the nanocomposite scaffold. All the samples were kept in a vacuum desiccator at room temperature before any measurements.

2.3 Physical and mechanical characterizations of pure chitosan and chitosan–HNTs NC scaffolds

Viscosity measurement. Viscosities of chitosan solution and chitosan–HNTs solution were measured using a digital rotational viscometer, SNB-1 (Shanghai Hengping Instruments Ltd., China) at room temperature. The sensor was fixed at the center of the

solution (50 mL) contained in a glass vessel (35 mm in diameter and 60 mm length). Three measurements for every sample were performed and the average data of viscosity were used.

Atomic force microscopy (AFM). To evaluate the surface morphology of raw HNTs and chitosan–HNTs, a multimode AFM with NanoScope IIIa controller was used (Veeco Instruments). The dilute HNTs dispersion and chitosan–HNTs (1/1, w/w) solution were dispersed on a piece of freshly cleaved mica and images were collected under contact mode using a soft cantilever (NP-S20, Veeco, force constant *ca.* 0.1 nN nm^{-1}).

Transmission electron microscopy (TEM). The dilute HNTs aqueous dispersion and chitosan–HNTs aqueous solutions were dipped and dried on the carbon-film supported Cu-grid. Then the samples were observed using a Philips Tecnai 10 TEM under accelerating voltage of 100 kV. The elemental compositions of the interface phase of chitosan–HNTs samples were analyzed with an attached X-ray energy dispersive spectrometer (X-ray EDS) and the atomic ratios of the determined elements were given by INCA Energy software.

Fourier transform infrared spectroscopy (FTIR). The FTIR spectra of the scaffold samples were measured using attenuated total reflectance (ATR) using a MAGNA-IR760 (Nicolet Co, USA). ATR is a sampling technique used in conjunction with infrared spectroscopy which enables samples to be examined directly in the solid or liquid state without further preparation. Thirty-two consecutive scans were taken and their average was stored. Spectra were taken from 4000 to 400 cm^{-1}. The wavenumber resolution was 2 cm^{-1}.

Mechanical properties determinations. Compression testing of freeze-dried chitosan and chitosan–HNTs scaffolds was carried out using a Zwick/Roell Z005 machine at 25 °C according to ISO 844 : 2007. The samples for the test were cylindrical samples with a diameter of 10 mm and thickness of 10 mm. The crosshead speed was 2 mm min^{-1}, and the tests proceeded up to failure or until 95% reduction in specimen height. The stress–strain curves for every sample were recorded automatically. The compressive modulus was calculated as the slope of the initial linear portion of the stress–strain curve. At least five samples were used to obtained reliable data.

Scanning electron microscopy (SEM). Before SEM observation, the scaffolds were sectioned and sputter coated with a 10 nm thick gold–palladium layer using a sputter coater (BALTEC SCD 005). The morphology of the scaffolds was observed with a Philips XL30 ESEM and Hitachi S-4800 FE-SEM (for high magnification photos).

Thermogravimetric analysis (TGA). TGA of the chitosan and chitosan–HNTs NC scaffold was carried out with a NETZSCH TG 209 F3 Tarsus® from room temperature to 600 °C at a heating rate of 10 °C min^{-1} under N_2 atmosphere. This experiment was used to study the thermal degradation behavior of the scaffolds.

X-ray diffraction (XRD). XRD profiles for samples were obtained using an X-ray diffractometer (D8, Bruker Corporation) at room temperature. The CuKα radiation source was operated at 40 kV power and 40 mA current. The wavelength of the X-ray beam was 0.15418 nm, and the layer spacing of the samples were calculated according to the Bragg's equation. The scanning angle was from 2° to 50°.

Porosity measurement. The total porosity was determined by the procedure as follows.[12] Firstly, the volume and weight of the scaffolds were measured and noted as V_0 and W_0, respectively. Secondly, the density (ρ) of the corresponding non-porous pure chitosan film and chitosan–HNTs nanocomposite films was determined by measuring their weight and volume. Finally, the porosity of the sample was calculated based on the following formula,

$$\text{Porosity } (\%) = \left[\frac{V_0 - \left(\frac{W_0}{\rho}\right)}{V_0}\right] \times \%$$

Three parallel sets were analyzed for every scaffold and the mean value of the porosities of different scaffolds was taken.

Water uptake abilities. The water uptake ability (E_A) of a scaffold was studied using the following procedure. Dry scaffolds were weighed (W_{dry}) and immersed in distilled water for 48 h. Then the scaffolds were gently removed from the beaker after 48 h and placed on a wire mesh rack. Excessive water was drained and scaffolds were weighed (W_{wet}) to determine water uptake.

$$E_A = \left[\frac{W_{wet} - W_{dry}}{W_{dry}}\right] \times \%$$

2.4 *In vitro* fibroblasts response on pure chitosan and chitosan–HNTs nanocomposites

Cell culture. The cytotoxicity of the chitosan and chitosan–HNTs nanocomposites was investigated by carrying out a cellular viability assay (MTT test) and fluorescence microscopy using mouse fibroblastic-like cells *via* coating the chitosan and chitosan–HNTs nanocomposites on the culture plate wells. The diluted chitosan and chitosan–HNTs solutions were carefully dipped on the surface of the wells and then dried at 45 °C to form thin films. Afterwards, all the materials were treated with 2 wt% sodium hydroxide aqueous solution to remove excessive acetic acid, then rinsed with a good deal of distilled water and dried at 45 °C. Prior to cell culture, all the films were sterilized by exposure to UV light for 1 hour and washed by sterile phosphate buffer saline solution (PBS) three times. The NIH3T3 mouse fibroblast cell line was used in the experiments. Cells were cultured and passaged in regular culture media consisting of Dulbecco's modified eagle medium (DMEM) supplemented with 10 vol% fetal bovine serum (FBS) and the antibiotics penicillin (100 units per mL) and streptomycin (100 μL mL^{-1}). Cells were incubated at 37 °C in a 5% CO_2 incubator and the medium was changed every 3 days. Cells were routinely removed from the tissue culture polystyrene (TCPS) dish with 0.25% trypsin–EDTA and plated on different substrates. The seeding cell density of 96 well culture plates was 2.0×10^4 cell per mL.

Cell staining and observations. After 3 days of culture on the pure chitosan film and chitosan–HNTs films, cells were rinsed carefully with warm PBS to remove non-adherent cells. All samples were fixed with 4% paraformaldehyde in PBS for 30

min and then permeabilized with 0.1% v/v Triton X-100 for 5 min. For fluorescence staining, the cells were incubated with 1 mg mL^{-1} phalloidin-TRITC (Sigma) for 1 h at room temperature to label the filamentous actins. Once thoroughly rinsed, nuclei were stained with 5 mg mL^{-1} 4′,6-diamidino-2-phenylindole (DAPI, Sigma) for 15 min. All the stained samples were rinsed extensively with PBS, prior to observation under an immunofluorescence microscope (IX71, Olympus) mounted with a CCD.

Cell viability assay. Cell proliferation on the pure chitosan and chitosan–HNTs nanocomposites was assessed by dimethylthiazol diphenyltetrazolium bromide (MTT) assay. Cells were seeded at a density of 2×10^3 cells per well onto the equilibrated membranes in 96-well cell culture plates and were incubated at 37 °C in a 5% CO_2 incubator. At the time points of 1, 4 and 7 days, 10 μL MTT solution (5 mg mL^{-1}) was added to each well. After incubation for 4 h at 37 °C, the upper medium was removed carefully and the intracellular formazan was dissolved by adding 100 μL dimethyl sulfoxide (DMSO) to each well. Then the solutions were agitated by a shaker for 15 min. The absorbance was measured at 570 nm using a spectrophotometric microplate reader (Bio-Rad, Model 550, USA). Experiments were run in triplicate per sample. The cells inoculated directly on TCPS were regarded as a negative control. All data were expressed as the mean ± standard deviation (SD) for $n = 3$.

3 Results and discussion

3.1 Interactions between HNTs and chitosan

Chitosan was utilized as the scaffold material in the current study due to its good biocompatibility and biodegradability, and it is an environmentally friendly material. Attributed to the electrostatic attraction and hydrogen bonding interactions between chitosan and HNTs, the inorganic nanotubes can be uniformly dispersed in chitosan aqueous solution by simply stirring without using a stabilizer. The viscosity of the resulting chitosan–HNTs suspension was determined by a rotational viscometer and the data are plotted in Fig. 1. Compared with the pure chitosan solution, the viscosity of chitosan–HNTs suspensions slightly decreased initially and then gradually increased. When the content of HNTs in the chitosan–HNTs dispersion is relatively low (33.3 wt% of CS2N1), the viscosity slightly decreased compared with that of the pure chitosan solution. This can be explained by the fact that the small amount of HNTs can break the networks formed by chitosan chains *via* inter/intra molecular interactions. The decreased inter-molecular interactions of chitosan lead to the slightly decreased viscosity of the dispersion. However, when HNTs loading increases in chitosan–HNTs, the viscosity of HNTs dispersions cannot be ignored and it dominates the viscosity increase of the dispersion. As a result, the viscosity gradually increases and reaches a maximum value of 1600 mPa s for the dispersion with 80 wt% HNTs. With further increase in the content of HNTs, the viscosity of the chitosan–HNTs dispersion increases significantly. As a consequence, it is hard to process these mixture dispersions, such as casting the suspension to a mould. The homogeneous chitosan–HNTs dispersions are freeze-dried at −86 °C in a freezer, giving rise to self-supported sponge-like 3D porous scaffolds, as shown in the inset of Fig. 1. The scaffolds retained the cylindrical shape of the mould they were freeze-dried in without sample shrinkage being observed. The shape and appearance of chitosan–HNTs NC scaffolds are not dependent on the sample composition, which indicates that HNTs have no effect on the formation of chitosan porous scaffolds.

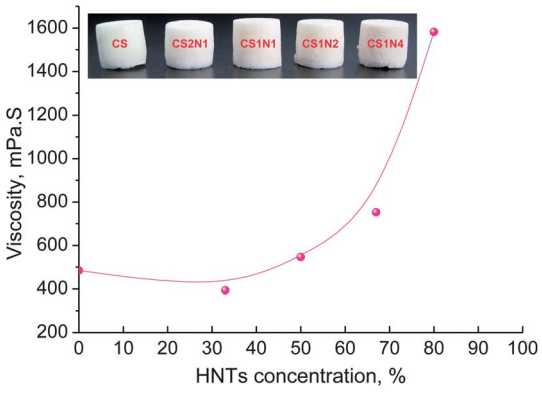

Fig. 1 Viscosity of chitosan solution and chitosan–HNTs dispersions (the inset shows the appearance of corresponding freeze-dried scaffolds).

Previously, the interfacial interactions between HNTs and chitosan have been confirmed in nanocomposite films.[22] Both the electrostatic attractions and hydrogen bonding are responsible for the uniform dispersion of HNTs in chitosan matrix and the enhancement of the performance of the nanocomposites. Chitosan is positively charged in the acidic solution due to the protonation of the amines. In contrast, HNTs are negatively charged due to isomorphous substitution of Al^{3+} for Si^{4+}.[19] As a result, mixing chitosan with HNTs results in the electrostatic attraction between them. In addition, the amine groups and hydroxyl groups on the chitosan can interact with the Si–O bonds and/or hydroxyl groups of HNTs *via* hydrogen bonding interactions. In the prepared chitosan–HNTs NC scaffolds, the hydrogen bonding interactions between HNTs and chitosan are also confirmed. Fig. 2 shows the FTIR spectra in the range of 1200–1800 cm^{-1} and 800–1300 cm^{-1} of HNTs, chitosan scaffold, and chitosan–HNTs NC scaffolds. As shown in Fig. 2(a), in the spectrum of chitosan, there are two characteristic peaks at 1545 cm^{-1} and 1403 cm^{-1}, which are assigned to the deformation vibrations of the protonated amine group ($-NH_3^+$) and hydroxyl group, respectively.[11,24] The two peaks for the chitosan–HNTs nanocomposites slightly shift to higher frequencies (*i.e.* the absorbance bands of NH_2 and OH vibrations move from 1545 and 1403 to 1550 and 1409 cm^{-1}, respectively, for the CS1N2), which is attributed to the electrostatic interactions and H-bonding interaction between the nanotubes and chitosan. Another evidence for the formation of hydrogen bonding is the changes of the peaks in the range of 800–1300 cm^{-1}, as shown in Fig. 2(b). For HNTs, two peaks around 1031 cm^{-1} and 910 cm^{-1} are attributed to in-plane Si–O stretching and O–H deformation of inner hydroxyl groups.[25] In the spectrum of chitosan, the peak around 1020 cm^{-1} is assigned to the

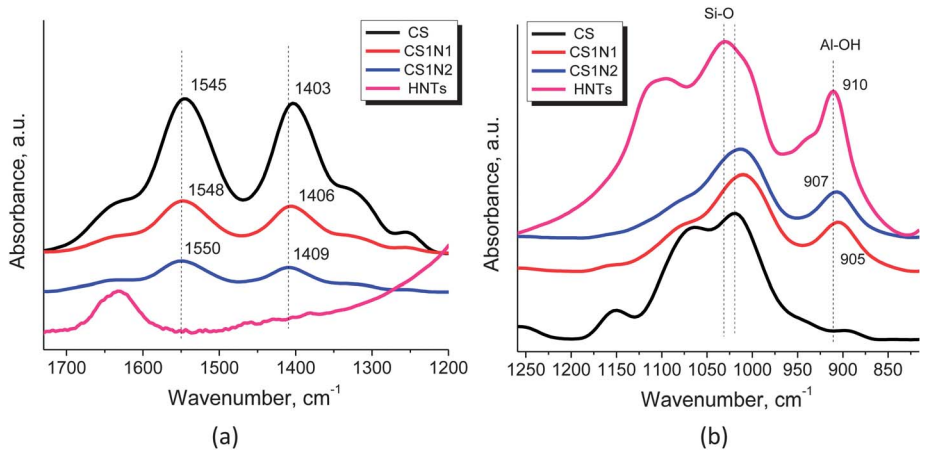

Fig. 2 ATR-IR spectra of HNTs, chitosan and chitosan–HNTs NC scaffolds: (a) 1200–1800 cm^{-1} and (b) 800–1300 cm^{-1}.

vibration of the C–O bond.[26] However, the peaks around 1031 cm^{-1} and 910 cm^{-1} move to lower wavenumbers in the chitosan–HNTs nanocomposites. This shift is also induced by the hydrogen bonding interactions between HNTs and chitosan. The previous zeta potential measurement results also confirmed the electrostatic attraction interactions between HNTs and chitosan.[22]

The interactions between HNTs and chitosan can result in absorption of chitosan chains on the surfaces of HNTs. We utilized AFM and TEM techniques to observe the absorption behavior of chitosan on HNTs. Fig. 3 presents AFM height images of the surface morphology for pristine HNTs and chitosan–HNTs. One can see that HNTs have cylindrical-shaped tubular morphology and open-ended lumen along the nanotubes (Fig. 3(a)). The walls of the pristine tubes are clean and smooth. For the chitosan–HNTs, however, the walls of HNTs are rough and indistinct. On the whole, the edge of HNTs is clear and sharp while the edge of chitosan–HNTs is obscure and blurred. From the TEM photos of chitosan–HNTs in Fig. 4(b), an organic layer with light gray color, which is about 20 nm thick,

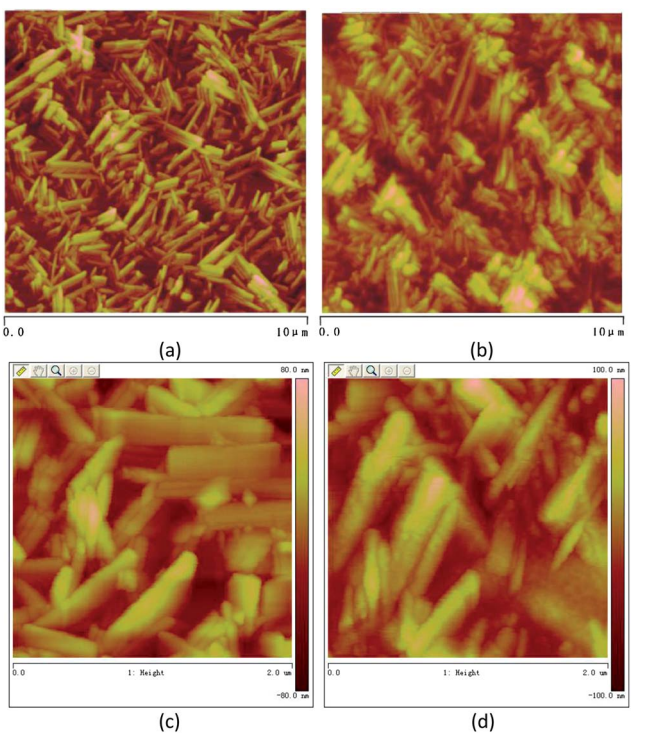

Fig. 3 AFM images of HNTs and chitosan–HNTs (50 wt% HNTs): (a and c) HNTs; (b and d) chitosan–HNTs. The samples were prepared by dipping the dilute HNTs and chitosan–HNTs aqueous dispersions on freshly clean mica.

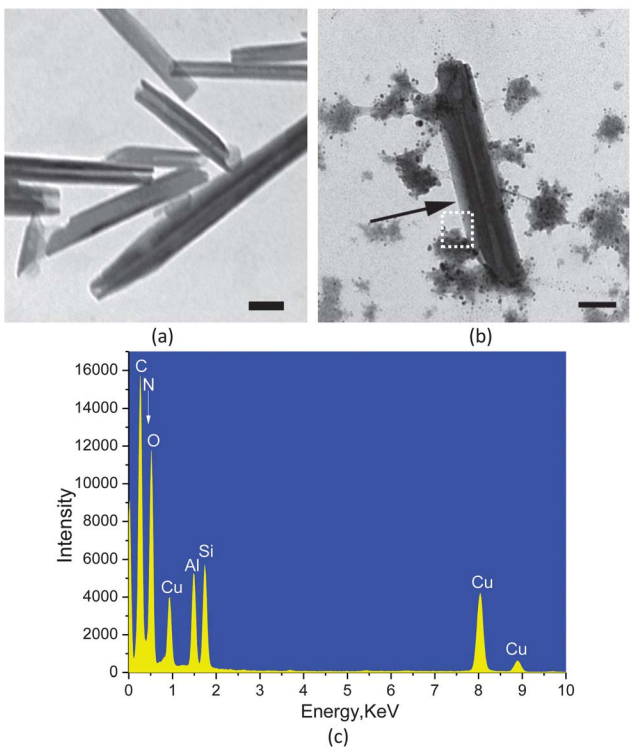

Fig. 4 TEM images of (a) raw HNTs and (b) chitosan–HNTs and X-ray EDS spectrum of the chitosan–HNTs interface phase shown in the box in (b). The bars in the TEM photos represent 100 nm and the arrow indicates the location of the chitosan layer absorbed on the nanotube.

is found to be located on the outer surfaces of HNTs. Thus the TEM image in Fig. 4(b) provides the most direct evidence for the presence of the chitosan on the nanotube surfaces. Generally, the polymer phase is not electron dense and cannot be identified under TEM observation. But when the polymer layer is thick enough, one can observe it. The wrapping of polymer layer around nanotube has also been found in other polymer–nanotube hybrid systems.[27,28] The chemical composition of the organic layer was analyzed by X-ray EDS spectroscopy and the result is given in Fig. 4(c). The chemical composition of the interface phase for chitosan–HNTs sample is C(58.6%), N(1.8%), O(27.4%), Al(4.3%), Si(4.4%) and Cu(3.5%). The Cu element comes from the Cu grids used as the sample support in TEM observation. The Al, Si and part of the O come from the HNTs, since the chemical composition of raw HNT is Al(18.5%), Si(19.1%) and O(62.2%).[29] As C and N are the characteristic elements of chitosan, the interface phase in the chitosan–HNTs consists of largely chitosan and little HNTs. Therefore, the organic layer in Fig. 4(b) is composed mainly of chitosan. All the observations strongly suggest that chitosan can be absorbed on the outer surface of HNTs when they come into close contact in the solution. The driving force for absorption is attributed to the interfacial interactions between chitosan and HNTs, as illustrated above. Actually, chitosan absorbed on other silicate clays has also been reported previously.[30,31]

3.2 Compression property of chitosan–HNTs NC scaffolds

The pure chitosan scaffold obtained by lyophilization method is relatively weak, which hinders their applications in tissue engineering since the scaffold must be easily handled and must be able to support a modest load during cell culture. The weak mechanical performance of the chitosan scaffold mainly arises from both the low Young's modulus of chitosan and low density of the formed scaffold. To improve the mechanical properties, incorporation of nano-scaled reinforcements in the preparation of NC scaffolds is an effective method.[9,16] Fig. 5 shows the typical compression stress–strain curves for pure chitosan and chitosan–HNTs NC scaffolds. Table 1 summarizes the compressive stress at 80% strain, compressive modulus and plateau stress data of the chitosan and chitosan–HNTs NC scaffolds. It can be seen that the curves of all samples clearly showed three discrete regions with characteristics of a low density elastomeric foam in compression: namely a linear elastic regime (between 0 and ~10% strain) caused by internal pore bending, a collapse plateau regime (~10 to ~60% strain) due to pore buckling or collapse and a densification regime (~60 to ~100% strain) due to complete pore collapse throughout the material.[32] The pure chitosan scaffold is soft, spongy and elastic, and the overall strength is generally low, around 0.16 MPa. The data are comparable with previous reported data of chitosan scaffolds.[9,33] By incorporation of HNTs, the stress of the NC scaffold samples is significantly higher than that of pure chitosan at all the tested strains. The increasing trend of stress is also proportional to the loading of HNTs. For example, the stress at 80% strain for CS1N4 is 0.55 MPa, which is about 17 times higher than that of the pure chitosan scaffold. Also the compression modulus of NC scaffolds is significantly higher than that of pure chitosan. The maximum compression modulus of the NC scaffold is 450.6 kPa with 80 wt% HNTs which is higher than that of previously reported chitosan–HA NC scaffolds[8] and the data is comparable with that of chitosan–CNTs NC scaffolds.[9] The mechanical property values of porous scaffolds are related to the density of the scaffold and Young's modulus of the materials from which the scaffold is being made.[34] Greater relative density of scaffold and higher modulus of the materials can improve the measured mechanical properties of a scaffold. So, increasing the concentration of the chitosan solution and combining with well-dispersed nanofillers can result in the improvement of the compression performance. Incorporation of HNTs into chitosan can increase the density of the scaffold (shown below) due to the greater content of materials of the chitosan–HNTs dispersion. Meanwhile, HNTs can interact with chitosan *via* electrostatic attraction and hydrogen bonding as illustrated before, which leads to the improved Young's modulus of chitosan.[22] As a consequence, the compression property of chitosan–HNTs NC scaffolds significantly increases compared with that of pure chitosan scaffold. Therefore, since the chitosan–HNTs nanocomposite scaffolds showed excellent, composition-dependent mechanical properties, they have potential application as tissue engineering supporting materials.

Table 1 Mechanical properties values of the chitosan–HNTs NC scaffolds (data in parentheses indicate the standard deviations)

Samples	Compressive stress at 80% strain (MPa)	Compressive modulus (E) (kPa)	Plateau stress[a] (kPa)
CS	0.030 (0.005)	34.9 (0.3)	6.06 (0.05)
CS2N1	0.076 (0.007)	77.3 (0.5)	23.0 (0.03)
CS1N1	0.254 (0.004)	305.3 (0.7)	72.3 (0.07)
CS1N2	0.346 (0.010)	436.0 (1.2)	85.4 (0.06)
CS1N4	0.550 (0.008)	450.6 (0.9)	135.1 (0.08)

[a] The plateau stress is the stress at the collapse plateau regime for each compressive stress–strain curve.

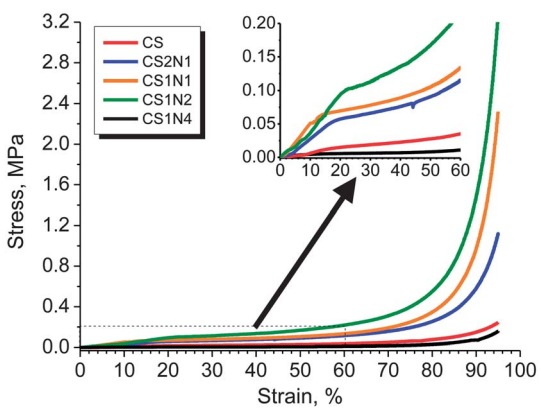

Fig. 5 Compressive stress–strain curves of chitosan and chitosan–HNTs NC scaffolds. Inset shows an expansion of the strain range 0–60%, showing compressive modulus change of the samples.

3.3 Microstructure of the chitosan–HNTs NC scaffolds

Fig. 6 exhibits representative cross-sectional structures of pure chitosan and chitosan–HNTs NC scaffolds fabricated using the freeze-drying technique. As observed, both pure chitosan scaffold and chitosan–HNTs NC scaffolds display a highly porous, open, and 3D interconnected morphology with the pore size around 200 μm. Addition of HNTs into chitosan has no significant influence on the microstructure of the scaffolds. So the NC scaffolds can also support cell in-growth and facilitate the exchange of nutrients and cellular waste products as well as the pure chitosan scaffold. However, the chitosan–HNTs NC scaffolds show more uniform porous structure and less collapse of the pore walls. This can be attributed to the enhanced pore formation ability of chitosan by HNTs due to the interactions that improve the stiffness and modulus of chitosan. The increased mechanical strength of the scaffold materials results in a more homogeneous porous structure and less collapse of the pore walls. Meanwhile, the NC scaffolds with HNTs have

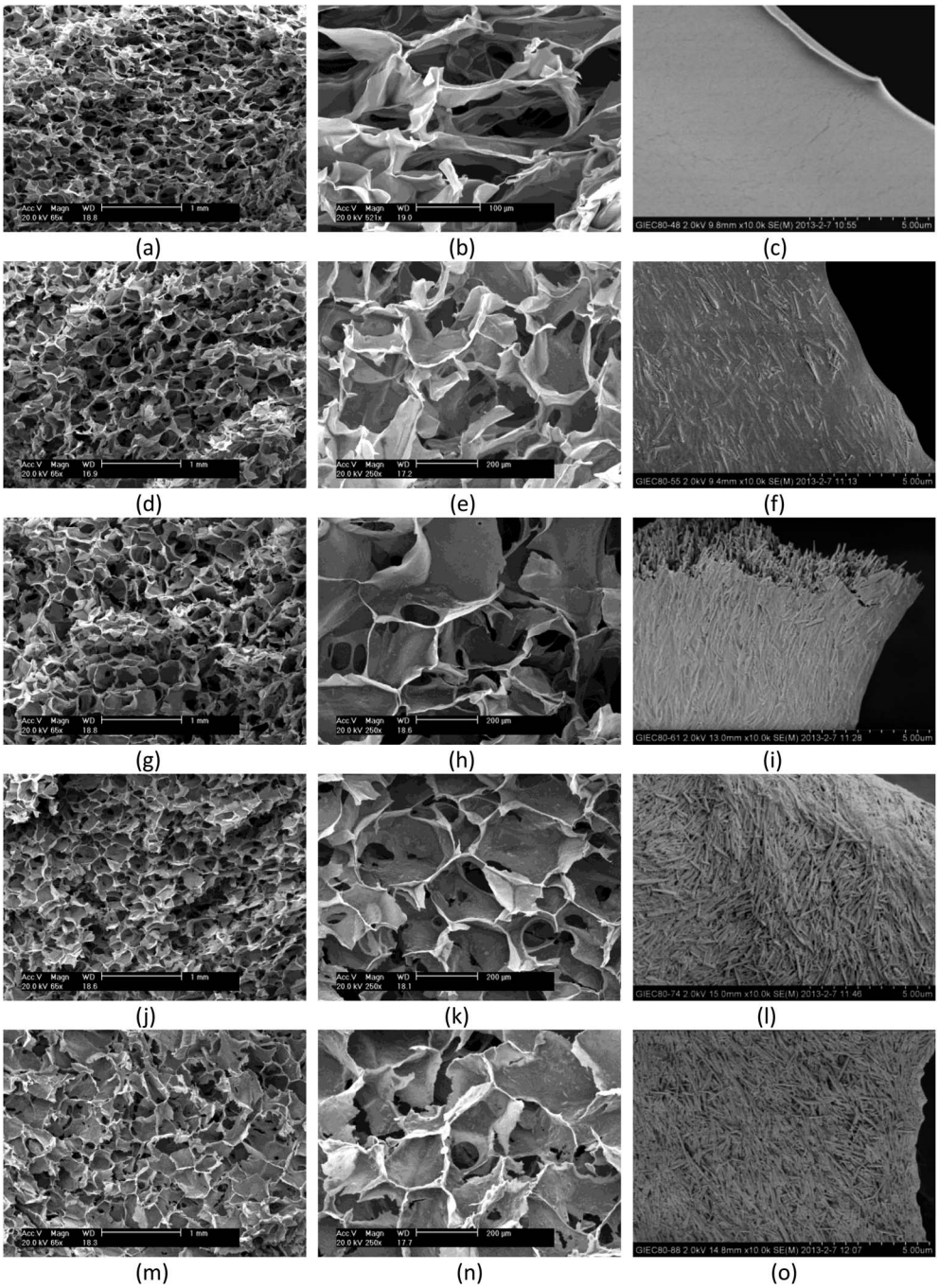

Fig. 6 SEM photos of freeze-dried chitosan and chitosan–HNTs NC scaffolds with different magnifications: pure chitosan (a–c); CS2N1 (d–f); CS1N1 (g–i); CS1N2 (j–l); and CS1N4 (m–o).

slightly larger pore sizes compared with that of the pure chitosan scaffold. This may be attributed to the much larger size of the initial ice crystals in the chitosan–HNTs nanocomposites which may result from the slightly decreased hydrophilicity of the nanocomposites. Nevertheless, all the pore sizes are sufficiently large to enable cell proliferation and a favorable spatial arrangement of cells, since the average size of fibroblast or osteoblasts is 10–30 μm. As observed from the high magnification SEM photos of the NC scaffolds in Fig. 6 and the EDS spectroscopy data (Fig. S1 and Table S1†), HNTs are exposed in the surfaces of the pores. The uniform distribution of HNTs in the chitosan matrix is also attributed to their interfacial interactions. The exposed HNTs in the pore wall lead to enhancement of the surface nanoroughness of the pores, which will further facilitate cell attachment and proliferation on the surfaces by acting as an anchor framework.[35] It can be concluded from the morphology results that the addition of HNTs in the chitosan matrix has no significant influence on the pore structure of the scaffolds. The prepared high-strength chitosan–HNTs NC scaffolds have potential application in tissue engineering due to their proper microstructure for cell attachment and development.

The microstructures of the NC scaffolds were further investigated by XRD. Fig. 7 compares the XRD patterns of HNTs, chitosan and chitosan–HNTs NC scaffolds. For pure chitosan, only a broad scattering reflection, locating at around $2\theta = 20^\circ$, is found in the XRD spectrum, indicating that it is amorphous. Raw HNTs exhibits diffraction peaks at $2\theta = 12^\circ$, 20°, and 25° which are assigned to (001), (02,11), and (020) planes of HNTs, respectively.[36] The basal reflection of 7.25 Å indicated that the used HNTs are dehydrated. The peak around 12° of HNTs in the NC scaffolds increases with the loading of HNTs, indicating the uniform mixing of chitosan and HNTs. The location of the diffraction peaks of HNTs in the NC scaffolds remained unchanged, indicating that no intercalation of chitosan into the interlayer of tube walls occurs. The chitosan chains with large molecular size might be blocked by strong hydrogen bonds among the sheets of the nanotubes. Interestingly, the intensity of the (001) reflection relative to the (02,11) band increases with the increase of HNTs loading, which indicates that a partial orientation of HNTs takes place in the NC scaffolds *via* the interfacial interactions with chitosan. The orientation of HNTs was also found in another polymer matrix or under pressure conditions.[36,37] From the XRD result, it can be concluded that HNTs can be uniformly distributed and partly oriented in the NC scaffolds but their layer space remains unchanged.

3.4 Density, porosity, and water uptake of the chitosan–HNTs NC scaffolds

Fig. 8 compares the density, porosity, and water uptake of the chitosan and chitosan–HNTs NC scaffolds. The pure chitosan scaffold has the lowest density among the samples, namely 8.38×10^{-3} g cm^{-3}. The density of the NC scaffolds is generally higher than that for pure chitosan and it linearly increases with HNTs concentration. The increased density of NC scaffolds is attributed to the greater material content in the same scaffold volume. As illustrated above, the higher the scaffold density is, the higher the compressive strength is. Therefore, the mechanical property of the NC scaffold is improved by the addition of HNTs. Furthermore, scaffold porosity is essential in intestinal tissue engineering in order to facilitate cell migration and the porosity also affects the mechanical properties of the scaffold. Generally, a decrease in porosity is accompanied by an increase in the mechanical strength, due to the homogeneity and more closely packed materials. From the figure, it can be seen all the scaffolds show a high porosity >96% and the porosity difference among the samples is less than 1.4%. Addition of HNTs has no significant effect on the porosity of the scaffold, which is consistent with the previous SEM result. Thus, in the present work the enhancement of the mechanical properties of the scaffold by HNTs cannot be attributed to the difference in the porosity. However, incorporation of HA into chitosan led to slightly decreased porosity of the scaffold.[38]

Water uptake of scaffolds is also important because the absorption of physiological fluid and the transfer of nutrients and metabolites occur through the scaffolds. As presented in Fig. 8, the pure chitosan scaffold has a water absorption of 24%, which is comparable with previously reported values.[17] The

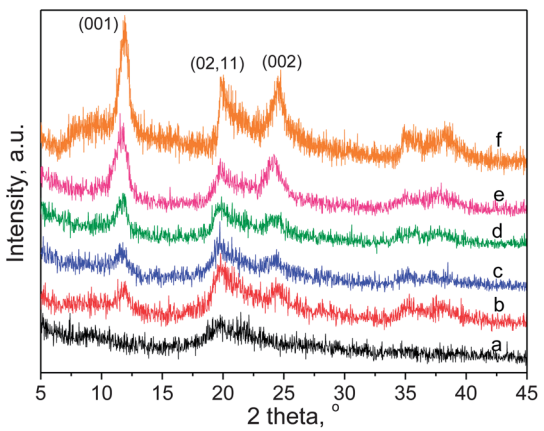

Fig. 7 XRD patterns for chitosan, HNTs and chitosan–HNTs NC scaffolds: (a) pure chitosan; (b) CS2N1; (c) CS1N1; (d) CS1N2; (e) CS1N4; and (f) HNTs.

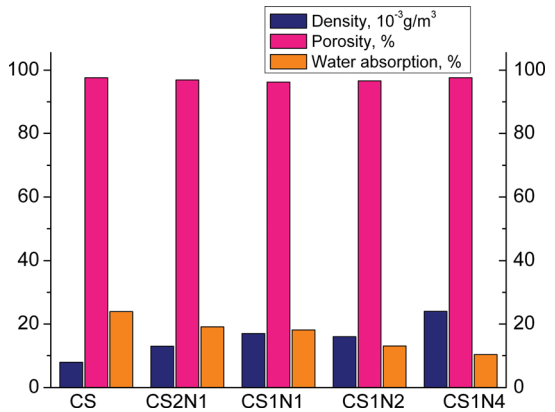

Fig. 8 Density, porosity and water absorption of freeze-dried CS and CS–HNTs composites scaffolds.

chitosan–HNTs NC scaffolds showed slightly decreased water uptake ratios compared with the pure chitosan scaffold. Incorporation of HNTs into the nanocomposites can result in a decrease in the polymer ratio of the scaffold. Since the water absorption of the clay is limited, it is considered that the water absorption property of the scaffold is primarily related to the water absorption of the polymer networks. As a result, the decreased polymer component in the nanocomposites results in a decreased water uptake ratio. In addition, the increase in HNTs loading leads to an increases in the crosslinking density of the NC scaffolds, which also results in decreased water absorption. Overall, these results suggest that the density, porosity and water absorption of chitosan–HNTs NC scaffolds are composition dependent and these properties can be tailored according to their applications in tissue engineering.

3.5 Thermal degradation of the chitosan–HNTs NC scaffolds

The interactions between HNTs and chitosan can also affect the thermal stability behavior of the NC scaffolds. The thermal stability of the chitosan and chitosan–HNTs NC scaffolds was studied by TG analysis (Fig. 9). From the TGA and DTG curves, three stages of decomposition of chitosan at around 70, 163, and 273 °C are observed, which are assigned to the loss of free water, loss of bonded water, and the degradation of the chitosan chains respectively. Only one peak around 483 °C is observed in HNTs, which is attributed to the structural dehydroxylation of HNTs.[19] By addition of HNTs, two peaks are observed in the chitosan–HNTs nanocomposites, which are assigned to the degradation of chitosan and HNTs, respectively. From the DTG curves, the degradation temperature of chitosan component is slightly increased compared to the pure chitosan, while the degradation temperature of HNTs component is slightly decreased compared to the pristine HNTs. For example, for the CS1N4 the degradation temperatures of chitosan and HNTs components are 277 °C and 477 °C, which are 4 °C higher and 6 °C lower than pure chitosan and pristine HNTs, respectively. This phenomenon is very similar to the compatible binary polymer blend systems in which the two glass transition values are dependent on the composition.[39] From the TGA results we thus can conclude that chitosan and HNTs are compatible and they have strong interfacial interactions in the nanocomposites.

3.6 *In vitro* cytotoxicity and cell proliferation of the chitosan–HNTs NC scaffolds

The potential of the chitosan–HNTs nanocomposite as cell scaffold materials for tissue engineering was investigated by evaluating the response of mouse fibroblast cells (NIH3T3) to the nanocomposites. We utilized the chitosan film and chitosan–HNTs nanocomposite films to investigate the *in vitro* cytocompatibility rather than the freeze-dried 3D scaffolds due to the following facts. Firstly, the *in vitro* cell experiment aims to investigate the influence of HNTs on the cytocompatibility of chitosan. Since the composition of chitosan and HNTs in the 2D films and 3D scaffolds is the same, the cytocompatibility results of the 2D films can be an indicator for the cell response of the corresponding 3D scaffolds. Secondly, the 2D films are more convenient for direct observation of the cell morphology compared with the corresponding 3D scaffolds, as the films of several micrometers are thinner and transparent. Thirdly, the sterilization process of the 3D scaffolds before cell culture by ^{60}Co γ-irradiation (even at 15 kGy doses) can significantly change the chemical structure, such as lowered molecular weight, and the physical structure, such as the surface morphology.[40,41] It is inappropriate to perform the cell experiments in scaffolds with totally different chemical and physical structures. While the sterilization process for the thin films is more convenient by exposure under UV light.

Firsty, the ability of the nanocomposite films to support attachment, viability and growth of the 3T3 cells was evaluated by observation of the cell morphology using fluorescence microscopy. The cells were seeded on chitosan and chitosan–HNTs nanocomposites coated wells and non-coated wells. As shown by the fluorescence images taken after three days culture (Fig. 10), the cells change from spherical to bipolar and exhibit good adhesion and extension on all the supported films. The cells were stained to label the nuclei (blue) and filamentous actins (red). From the nuclei photos, it can be seen that the cells are uniformly distributed on the materials. And from the merged photos, the cells spread to the whole areas of the

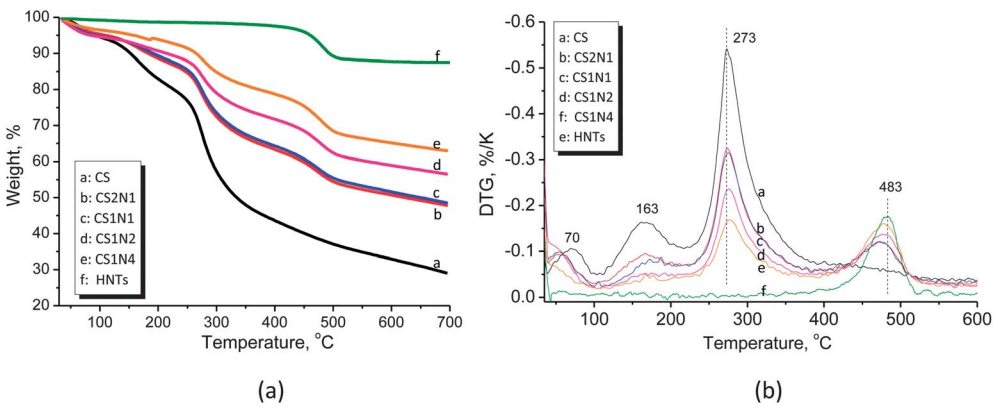

Fig. 9 TG (a) and DTG (b) curves for CS, HNTs and CS–HNTs NC scaffolds.

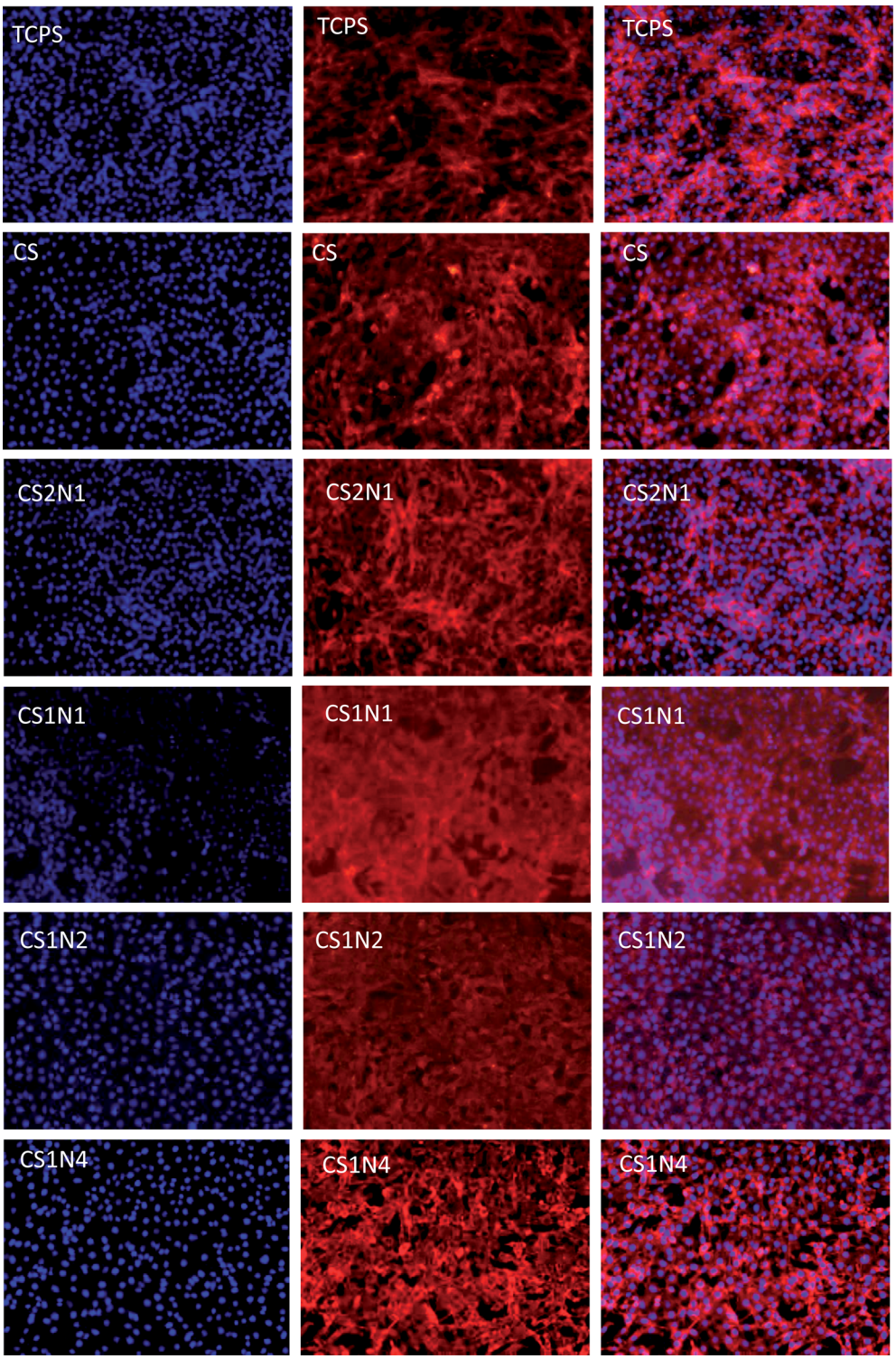

Fig. 10 Fluorescent micrographs of NIH3T3 cells on TCPS, pure chitosan and chitosan–HNTs nanocomposites after 3 days culture. The cells were stained to label the nuclei (DAPI, left column) and filamentous actins (phalloidin-TRITC, middle column). The last column shows the merged photo of the first two photos for the same sample.

materials after 3 days culture, indicating the materials are homogenous. It is hard to identify the difference among theses samples, suggesting that addition of HNTs has no significant effect on the cell attachment and development of chitosan. It is generally considered that the cell behavior on the materials depends on both the chemical composition and the topography of the surfaces. Incorporation of HNTs into chitosan leads to a change of chemical composition of the nanocomposites. For example, Si content increases because the external surface of HNTs is silica. The introduction of Si element in biomaterials is

beneficial for the improvement of bioactivities and osteoconductivity.[42–44] In addition, the slightly increased surface roughness of the chitosan by HNTs also contributed to the good cytocompatibility of the nanocomposites. Overall, the cytocompatibility of the present chitosan–HNTs nanocomposites is consistent with those previously reported systems.[45–47] For example, Vergaro *et al.* investigated the cytocompatibility of HNTs using cervical adenocarcinoma (HeLa) and breast cancer cells (MCF-7) and observed the uptake process of HNTs by the cells using confocal laser scanning microscopy.[45] Their results showed that HNTs were nontoxic to the cells and increasing HNTs concentration in aqueous dispersion was even much less harmful to cells than NaCl. Addition of HNTs into polyvinyl alcohol (PVA),[46] poly(lactic-*co*-glycolic acid) (PLGA),[47] and chitosan[22] also shows little effect on the biocompatibility of the polymers. From the cell morphology result, one can conclude that the chitosan–HNTs nanocomposites have a similar bioactivity to pure chitosan and can be used as supporting materials in tissue engineering.

We further used the MTT method to quantify the cell viability on the chitosan and chitosan–HNTs nanocomposites. The viability of NIH3T3 cells exposed to pure chitosan and chitosan–HNTs nanocomposites with different HNTs concentrations is summarized in Fig. 11. The results reveal that 3T3 cells can adhere and proliferate on both pure chitosan and chitosan–HNTs. After 1 day culture, the nanocomposites with relatively high HNTs concentration show a significantly increased optical density (OD) value, indicating the incorporation of HNTs into chitosan facilitates cell attachment and spread at early days. With increasing culturing time to 4 days, the OD value for the samples increases, suggesting the good development of the cells. After 7 days culture, the cells on the chitosan and the nanocomposites with low HNTs concentration have continued growth and cell viability of all the samples shows nearly no difference. This suggested that chitosan–HNTs nanocomposites show comparable biocompatibility to pure chitosan. The slight reduction of OD value after 7 days culture for CS1N2 and CS1N4 samples can be attributed to part of cells on these materials may be dead from little space and nutrition for growth. However, the OD values of both pure chitosan and the chitosan–HNTs nanocomposites are lower than that of the control sample (TCPS) especially at the early days. This can be attributed to the more hydrophobic character of TCPS compared with chitosan and nanocomposite films, since cell adhesion proteins tend to bind to the hydrophobic surface. The decreased cell viability of chitosan surfaces compared with the TCPS has also been reported.[48] Overall, the chitosan–HNTs nanocomposites show significantly improved physico-chemical and biological properties compared with the pure chitosan. Due to its versatile features of high mechanical strength, high porosity, improved thermal stability, and good biocompatibility, the chitosan–HNTs NC scaffolds have potential applications in tissue engineering and as drug/nucleic acid carriers.

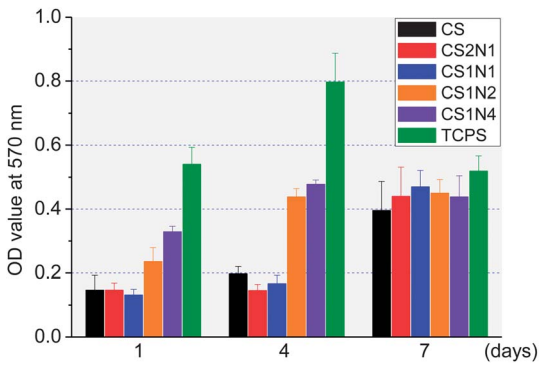

Fig. 11 Cell proliferation of NIH3T3 cells on chitosan and chitosan–HNTs nanocomposites as a function of time, measured by MTT assay, which represents active mitochondrial activity of living cells. Results expressed as means ± standard deviation.

4 Conclusions

Chitosan–HNTs NC scaffolds were prepared *via* solution mixing and freeze-drying method. The hydrogen bonding and electrostatic attraction between chitosan and HNTs were confirmed by spectroscopy and morphology analysis. The interfacial interactions resulted in a layer of chitosan absorbed on the surfaces of HNTs. The chitosan–HNTs NC scaffolds exhibited significantly enhanced compressive strength, compressive modulus, and thermal stability compared with the pure chitosan scaffold. But the NC scaffolds also showed reduced water uptake and increased density by incorporation of HNTs. All the scaffolds exhibited a highly porous structure and HNTs did not significantly affect the pore structure and porosity of the scaffolds. Cytotoxicity results showed these materials do not exert any cytotoxic effect to the NIH3T3 cells. Cell morphology results showed that cells can be attached and developed well on all of the materials. The present results develop the relationship between the microstructure and the physicochemical and biological properties of chitosan–HNTs NC scaffolds, which exhibited great potential for their use in tissue engineering strategies and as drug/nucleic acid carriers.

Acknowledgements

This work was financially supported by the Research Fund for the Doctoral Program of Higher Education of China (grant no. 20114401120003), the Key project of department of education of Guangdong province (no. cxzd1108), and the Key Laboratory of High Performance and Functional Polymeric Materials (South China University of Technology), Guangdong province, PR of China. The authors also thank Dr Hau-To Wong for reading and revising of the manuscript.

References

1 G. Chen, T. Ushida and T. Tateishi, *Macromol. Biosci.*, 2002, **2**, 67–77.
2 S. J. Hollister, *Nat. Mater.*, 2005, **4**, 518–524.
3 D. W. Hutmacher, *Biomaterials*, 2000, **21**, 2529–2543.
4 A. S. Hoffman, *Adv. Drug Delivery Rev.*, 2002, **54**, 3–12.

5 L. A. Smith and P. X. Ma, *Colloids Surf., B*, 2004, **39**, 125–131.
6 K. Lee, D. Kaplan, J. Velema and D. Kaplan, Biopolymer-Based Biomaterials as Scaffolds for Tissue Engineering, in *Tissue Engineering I*, Springer Berlin Heidelberg, 2006, vol. 102, pp. 187–238.
7 S. V. Madihally and H. W. T. Matthew, *Biomaterials*, 1999, **20**, 1133–1142.
8 W. W. Thein-Han and R. D. K. Misra, *Acta Biomater.*, 2009, **5**, 1182–1197.
9 L. J. Sweetman, S. E. Moulton and G. G. Wallace, *J. Mater. Chem.*, 2008, **18**, 5417–5422.
10 R. Jayakumar, R. Ramachandran, V. V. Divyarani, K. P. Chennazhi, H. Tamura and S. V. Nair, *Int. J. Biol. Macromol.*, 2011, **48**, 336–344.
11 W. Tan, Y. Zhang, Y. Szeto and L. Liao, *Compos. Sci. Technol.*, 2008, **68**, 2917–2921.
12 D. Depan, P. K. C. Venkata Surya, B. Girase and R. D. K. Misra, *Acta Biomater.*, 2011, **7**, 2163–2175.
13 C. K. S. Pillai, W. Paul and C. P. Sharma, *Prog. Polym. Sci.*, 2009, **34**, 641–678.
14 M. Rinaudo, *Prog. Polym. Sci.*, 2006, **31**, 603–632.
15 K. Rezwan, Q. Z. Chen, J. J. Blaker and A. R. Boccaccini, *Biomaterials*, 2006, **27**, 3413–3431.
16 J. Li, H. Sun, D. Sun, Y. Yao, F. Yao and K. Yao, *Carbohydr. Polym.*, 2011, **85**, 885–894.
17 M. Peter, N. S. Binulal, S. Soumya, S. V. Nair, T. Furuike, H. Tamura and R. Jayakumar, *Carbohydr. Polym.*, 2010, **79**, 284–289.
18 D. Depan, B. Girase, J. S. Shah and R. D. K. Misra, *Acta Biomater.*, 2011, **7**, 3432–3445.
19 E. Joussein, S. Petit, J. Churchman, B. Theng, D. Righi and B. Delvaux, *Clay Miner.*, 2005, **40**, 383–426.
20 X. Sun, Y. Zhang, H. Shen and N. Jia, *Electrochim. Acta*, 2010, **56**, 700–705.
21 Y. Zheng and A. Wang, *J. Macromol. Sci., Part A: Pure Appl. Chem.*, 2010, **47**, 33–38.
22 M. Liu, Y. Zhang, C. Wu, S. Xiong and C. Zhou, *Int. J. Biol. Macromol.*, 2012, **51**, 566–575.
23 D. G. Shchukin, G. B. Sukhorukov, R. R. Price and Y. M. Lvov, *Small*, 2005, **1**, 510–513.
24 A. Pawlak and M. Mucha, *Thermochim. Acta*, 2003, **396**, 153–166.
25 P. Yuan, P. D. Southon, Z. Liu, M. E. R. Green, J. M. Hook, S. J. Antill and C. J. Kepert, *J. Phys. Chem. C*, 2008, **112**, 15742–15751.
26 J. D. Schiffman and C. L. Schauer, *Biomacromolecules*, 2006, **8**, 594–601.
27 V. A. Sinani, M. K. Gheith, A. A. Yaroslavov, A. A. Rakhnyanskaya, K. Sun, A. A. Mamedov, J. P. Wicksted and N. A. Kotov, *J. Am. Chem. Soc.*, 2005, **127**, 3463–3472.
28 N. A. Kumar, A. Bund, B. G. Cho, K. T. Lim and Y. T. Jeong, *Nanotechnology*, 2009, **20**, 225608.
29 E. Abdullayev, A. Joshi, W. Wei, Y. Zhao and Y. Lvov, *ACS Nano*, 2012, **6**, 7216–7226.
30 X. Wang, S. P. Strand, Y. Du and K. M. Varum, *Carbohydr. Polym.*, 2010, **79**, 590–596.
31 H.-B. Yao, Z.-H. Tan, H.-Y. Fang and S.-H. Yu, *Angew. Chem., Int. Ed.*, 2010, **49**, 10127–10131.
32 B. A. Harley, J. H. Leung, E. C. C. M. Silva and L. J. Gibson, *Acta Biomater.*, 2007, **3**, 463–474.
33 Y. Zhang and M. Zhang, *J. Non-Cryst. Solids*, 2001, **282**, 159–164.
34 I. Keun Kwon, S. Kidoaki and T. Matsuda, *Biomaterials*, 2005, **26**, 3929–3939.
35 N. Gadegaard, E. Martines, M. O. Riehle, K. Seunarine and C. D. W. Wilkinson, *Microelectron. Eng.*, 2006, **83**, 1577–1581.
36 G. W. Brindley, K. Robinson and D. M. C. MacEwan, *Nature*, 1946, **157**, 225–226.
37 S. Rooj, A. Das, V. Thakur, R. N. Mahaling, A. K. Bhowmick and G. Heinrich, *Mater. Des.*, 2010, **31**, 2151–2156.
38 J. Venkatesan, Z.-J. Qian, B. Ryu, N. Ashok Kumar and S.-K. Kim, *Carbohydr. Polym.*, 2011, **83**, 569–577.
39 W. Brostow, R. Chiu, I. M. Kalogeras and A. Vassilikou-Dova, *Mater. Lett.*, 2008, **62**, 3152–3155.
40 J. Rosiak, P. Ulaski, M. Kucharska, J. Dutkiewicz and L. Judkiewicz, *J. Radioanal. Nucl. Chem.*, 1992, **159**, 87–96.
41 M.-S. Kim, Y.-J. Choi, H. S. Park and I. Noh, *J. Phys. Chem. Solids*, 2008, **69**, 1569–1572.
42 K. A. Hing, P. A. Revell, N. Smith and T. Buckland, *Biomaterials*, 2006, **27**, 5014–5026.
43 N. Patel, S. M. Best, W. Bonfield, I. R. Gibson, K. A. Hing, E. Damien and P. A. Revell, *J. Mater. Sci.: Mater. Med.*, 2002, **13**, 1199–1206.
44 A. E. Porter, N. Patel, J. N. Skepper, S. M. Best and W. Bonfield, *Biomaterials*, 2003, **24**, 4609–4620.
45 V. Vergaro, E. Abdullayev, Y. M. Lvov, A. Zeitoun, R. Cingolani, R. Rinaldi and S. Leporatti, *Biomacromolecules*, 2010, **11**, 820–826.
46 W. Y. Zhou, B. Guo, M. Liu, R. Liao, A. B. M. Rabie and D. Jia, *J. Biomed. Mater. Res., Part A*, 2009, **93**, 1574–1587.
47 R. Qi, R. Guo, M. Shen, X. Cao, L. Zhang, J. Xu, J. Yu and X. Shi, *J. Mater. Chem.*, 2010, **20**, 10622–10629.
48 K. S. Katti, D. R. Katti and R. Dash, *Biomed. Mater.*, 2008, **3**, 034122.